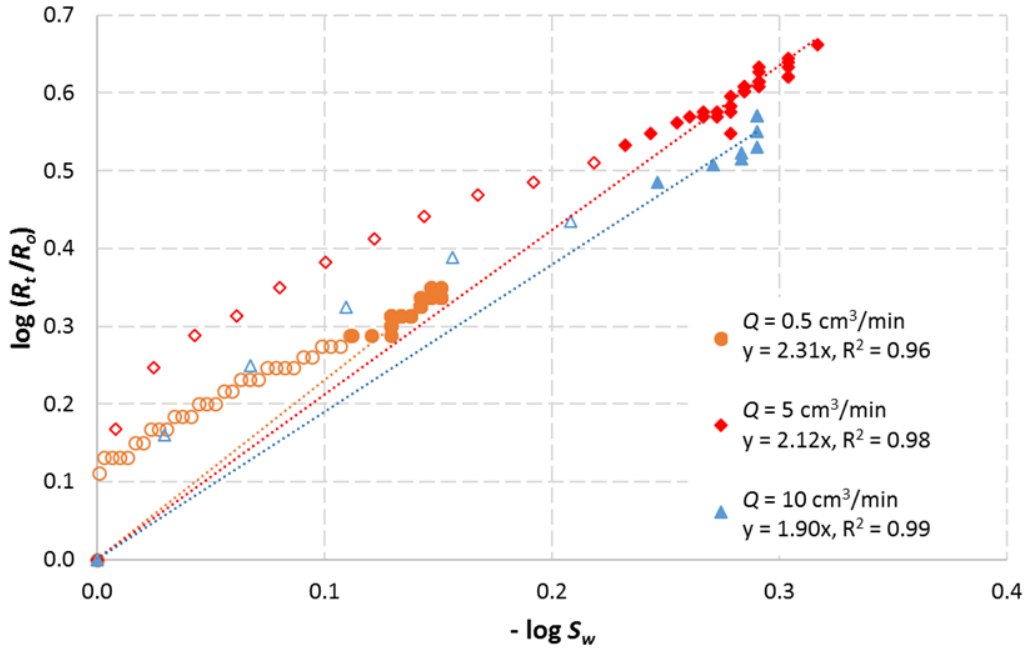

Fig 3. Logarithmic cross plot of RI and S_w during CO_2 injection in brine-filled Bentheimer core samples at injection rates: 0.5, 5 and 10 cm³/min at experimental conditions of 7.0 MPa and 20 °C. Data point markers with no fill (non-uniform saturation profile) were excluded from the linear trend lines. The saturation exponent n ranged between 1.9 – 2.3.

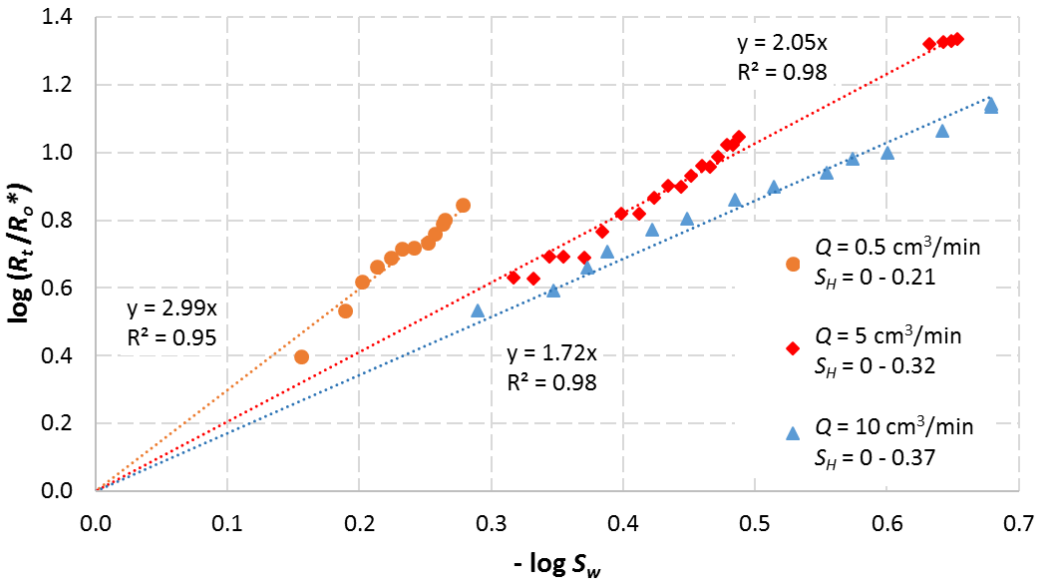

Fig 4. Logarithmic cross plot of RI and S_w during CO_2 hydrate formation in Bentheimer core samples from a range of initial brine saturations caused by varying CO_2 injection rates: 0.5, 5 and 10 cm³/min at 7.0 MPa and 4 °C. Depending on the saturation profiles, the saturation exponent n ranged from 1.7 to 3.0.

2.1 when S_H = 0.32 (S_w = 0.22), and 3.0 when S_H = 0.21 (S_w = 0.53). Compared to the CO_2-brine system, hydrate formation changed the n value for the 0.5 cm³/min drainage experiment (least uniform saturation distribution) from 2.3 to 3.0, for 10 cm³/min from 1.9 to 1.7, while for 5 cm³/min n remained unchanged (2.1). The dispersion in obtained saturation exponents increased with the additional complexity of hydrate formation and dynamic hydrate growth in the pore space. This caused the mean value of n to increase from 2.1 to 2.3 during CO_2 hydrate formation. The obtained n values are nonetheless in good agreement with recent studies for natural gas hydrate in coarse-grained reservoirs [13], and for glass bead specimen [23].

The next three figures show a direct comparison of saturation values derived from Archie's and from measured PVT data.

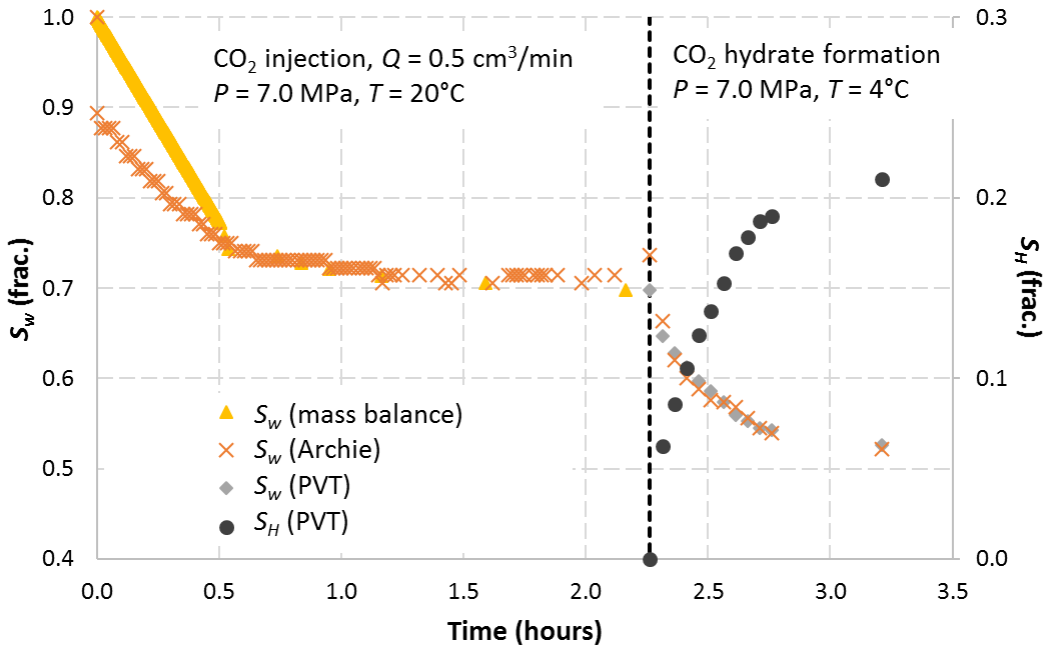

Fig 5. Comparison of saturation calculations from Archie and measured PVT data for injection rate 0.5 cm^3/min during initial displacement of water by CO_2 (7.0 MPa and 20 °C) and the following CO_2 hydrate formation (7.0 MPa and 4 °C). Obtained saturation values correlates very well after CO_2 breakthrough as a uniform saturation profile is established, and throughout CO_2 hydrate formation.

In Fig 5, saturation profiles during the initial displacement and the following hydrate nucleation and growth are displayed for flow rate 0.5 cm^3/min. The aforementioned unsteady-state regime occurring before CO_2 breakthrough, leads to severe deviation between the Archie saturation and correct linear displacement (mass balance) due to temporarily non-uniform saturation profiles. Once CO_2 breaks through at the outlet end of the sample, the saturation values from Archie's match actual PVT values very well at the plateau (S_w≈0.7). The onset of hydrate formation is indicated with a vertical line (broken). At this point, Archie's overestimate the water saturation somewhat compared to actual measurements. This apparent increase in water saturation is likely due to a short drop in resistivity linked to hydrate nucleation as reported in the literature [7,14,24]. Another possibility is the aforementioned CO_2 effects that may overestimate the water saturation, although the effects are most likely inhibited by the saline brine present. For the following hydrate growth process there is a very good agreement between the two water saturation profiles.

In Fig 6, drainage of water by CO_2 at injection rate of 5 cm^3/min and subsequent hydrate formation is displayed. Again, we observed a deviation in saturation profiles before CO_2 BT, and a good agreement after the CO_2 front reached the outlet end of the sample. The consistency continues from the onset of hydrate formation until hydrates occupy approximately 15% of the pore space. At this point the hydrate formation rate decreased substantially and the saturation profiles temporarily plateaued (for 0.2 hours). This period of hampered hydrate growth is not captured using Archie's saturation calculations, thus underestimating the water saturation here. Accelerated hydrate formation followed next and this "normalization" caused the end-point saturation values from PVT data and resistivity measurements to match once again.

Fig 7 shows saturation profiles during the initial displacement, and the following hydrate nucleation and growth for flow rate of 10 cm^3/min. The remaining water saturation in the core after CO_2 breakthrough was almost identical to the 5 cm^3/min experiment. There is a good agreement between the water saturation profiles after this point including the whole hydrate formation period in Fig 7.

CO_2 dissociation effects are highly sensitive to salinity. The 3.5 weight% NaCl solution used in Fig 5-7, belongs in a "high-salinity regime" where the conductivity was actually reduced by up to 15% due to reduced ion mobility [25]. This CO_2 dissolution effect, if not accounted for, will underestimate the water saturation derived from resistivity measurements. At the time-scale investigated in our study, no consistent impact of CO_2 dissociation on resistivity measurements was observed. Modifying Archie's equation by accounting for reduced effective porosity and increased salinity of the remaining water for each time step [14], resulted in resistivity saturation values agreeing very well with independent PVT measurements.

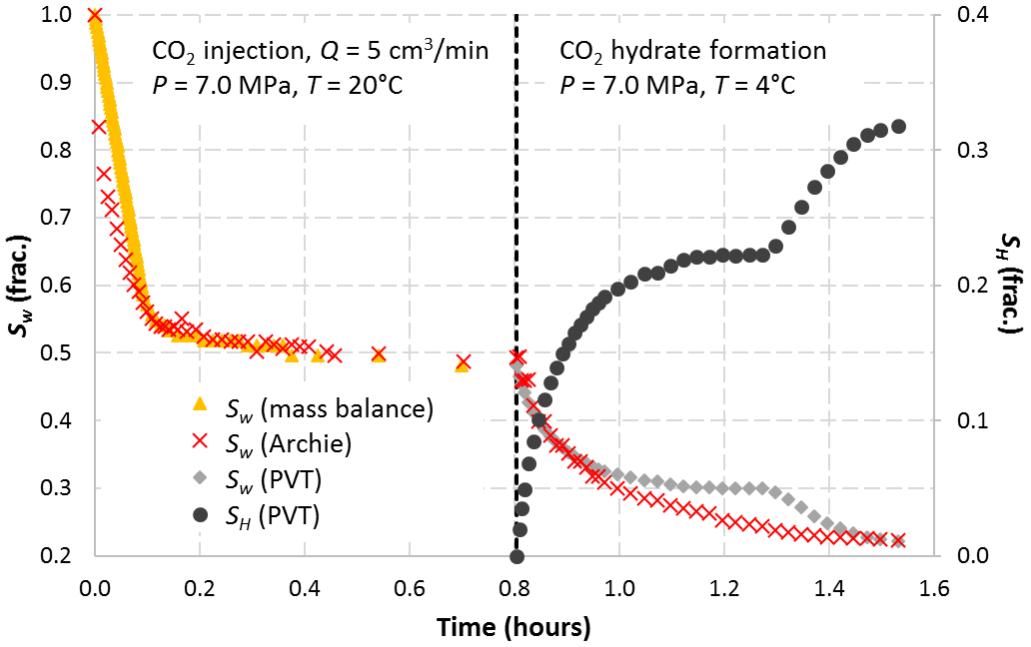

Fig 6. Comparison of saturation values obtained from Archie and measured PVT data for injection rate 5 cm^3/min during drainage (7.0 MPa and 20 °C) and during the following CO_2 hydrate formation (7.0 MPa and 4 °C).

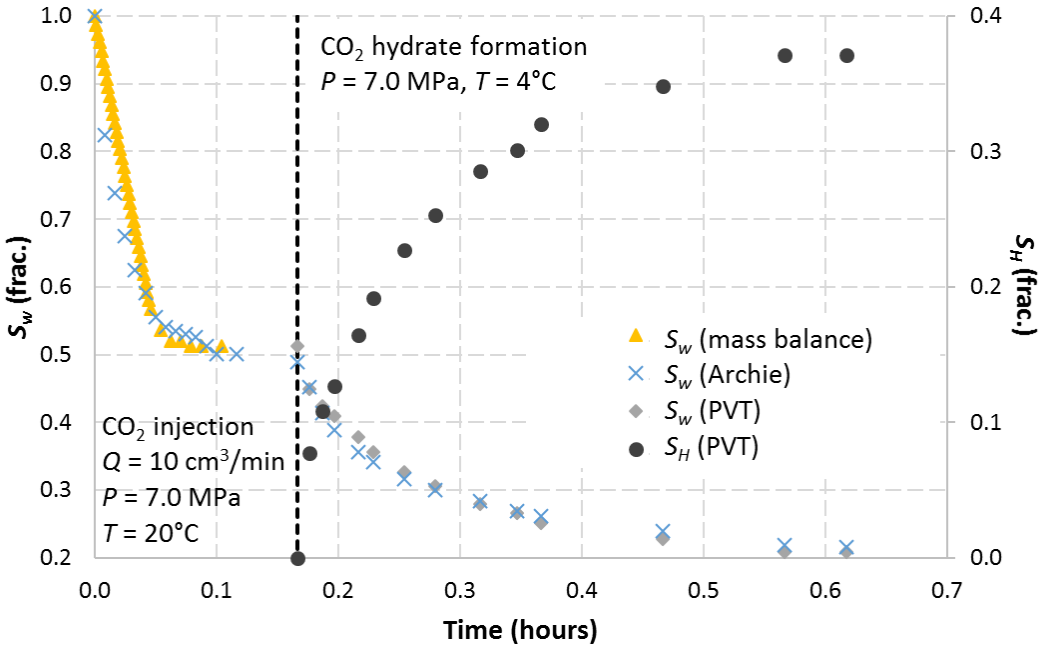

Fig 7. Comparison of saturation calculations from Archie and measured PVT data for injection rate 10 cm^3/min during initial displacement of water by CO_2 (7.0 MPa and 20 °C) and the subsequent CO_2 hydrate formation (7.0 MPa and 4 °C).

In addition to the constant pressure experiments, a series of flow-induced CO_2 hydrate formation experiments were tested for various thermodynamic conditions (within the GHSZ). CO_2 was injected into fully brine-saturated core samples at 7.0 MPa pore pressure and aquifer temperature of 4 °C or 6 °C. In Fig 8, resistivity profiles for different CO_2 flow rates, and salinity and temperature regimes are compared as a function of time. Here, increased flow rate (from 0.5 to 5 cm^3/min) accelerated hydrate formation and subsequent CO_2 trapping and immobilization. However, in terms of pore volumes (PV) CO_2 injected, we observed no effect of injection rate on hydrate induction time. The initial displacement of brine by liquid CO_2 increased the bulk resistivity from approximately 5 Ωm to 10 Ωm in all four corefloods. Two experiments were flooded with CO_2 at a constant rate of 5 cm^3/min at 7.0 MPa and 4 °C, where one core contained 3.5 weight% NaCl (red curve) and the other 5 weight% NaCl (yellow) – to demonstrate the effect of salinity increase on hydrate formation. Furthermore, two experiments were flooded with CO_2 at a constant rate of 0.5 cm^3/min at 7.0 MPa and salinity of 3.5 weight% NaCl, one experiment at 4 °C (blue) and the other at 6 °C (light blue) - to demonstrate the effect of temperature increase.

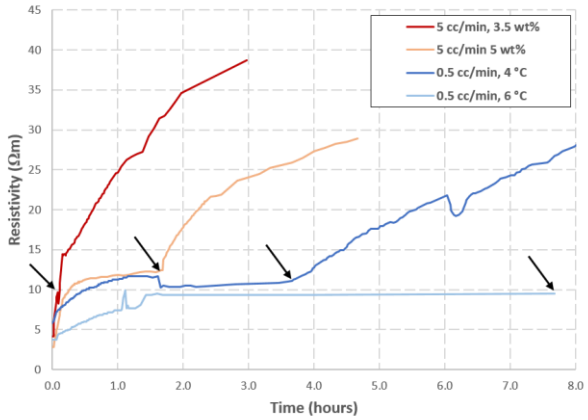

Fig 8. Resistivity profiles for various temperature and salinity conditions. Arrows indicate hydrate nucleation detected by a combination of pressure, resistivity, and temperature readings. Increase in salinity/temp caused a delayed CO_2 hydrate seal formation during continuous flow experiments.

The 5 cm^3/min constant rate experiment at lowest salinity (Fig 8 – red curve) started forming solid hydrates in the pore space shortly after CO_2 breakthrough (nucleation indicated with black arrows). By increasing the brine salinity from 3.5 to 5 weight% (yellow curve), we observed a prolonged induction time of approx. 1.5 hours (factor 9 increase) from flow-induced hydrate formation. When injecting CO_2 at 0.5 cm^3/min at 3.5 weight%, the effect of increasing the sandstone temperature from 4 °C to 6 °C was a factor 2 increase in induction time from 3.8 hours (blue) to 7.6 hours (light blue – resistivity data beyond this point is missing, however point of hydrate nucleation was identified from pressure and temperature logs).

The flow-induced hydrate induction time was evidently sensitive to salinity and temperature variations. All four experiments led to solid CO_2 hydrate formation eventually. The steady increasing resistivity profiles after nucleation demonstrated hydrate growth in the pore network and decreased effective porosity and permeability. All corefloods experienced significant differential pressure build-up across the samples after hydrate formation, effectively stopping the CO_2 production at the outlet. These observations suggest that the injected CO_2 phase is made discontinuous by pore-spanning hydrate layers acting as permeability barriers, and thus successfully obstruct viscous CO_2 flow in the core sample for the time investigated.

Conclusions

Electrical resistivity measurements providing fluid saturations relevant to CO_2 hydrate storage, resulted in the following key experimental observations:

For two-phase CO_2-brine systems, the saturation exponent n ranged from 1.9 – 2.3 (average n=2.1) depending on the CO_2 injection rate used during the drainage process. Because the saturation exponent is sensitive to the saturation profile along the core length, it is not recommended to rely on saturation values derived from resistivity measurements using a 2-electrode setup in non-uniform fluid distribution processes.

During CO_2 hydrate formation, the saturation exponent n ranged from 1.7 – 3.0 (average n=2.3) depending on the initial distribution of brine, which resulted in different final CO_2 hydrate saturations. The estimated values of n may be used to map the brine saturation S_w and the CO_2 hydrate saturation ($S_H = 1 - S_w$) in excess water conditions, and are in good agreement with previously measured n values during methane hydrate growth. Resistivity measurements are increasingly important for $S_H < 0.4$, as acoustic methods currently cannot obtain sufficient velocity contrasts in zones of low hydrate saturation.

CO_2 hydrates effectively blocked the CO_2 flow path and sealed off the sandstone pore network during flow-induced hydrate formation for different injection rates and thermodynamic conditions. Moderate increase in brine salinity or aquifer temperature resulted in significantly prolonged induction time before CO_2 hydrate formed under constant flow rate. Once stored, unwanted CO_2 re-mobilization/migration was obstructed by formation of sedimentary hydrate layers. This observed mechanism could act as an additional safety factor against leakage from geological stored CO_2 located below the gas hydrate stability zone.

The authors gratefully acknowledge financial support from Equinor and the Research Council of Norway. One of the authors is supported by CLIMIT grant number 255490.

Nomenclature

a = tortuosity constant
A = area, L^2, m^2
C = ion content of brine, ppm
F = formation factor
L = length, L, m
m = cementation exponent
n = Archie's saturation exponent
RI = resistivity index
R_o = resistivity of fully water saturated sample, $(mL^3)/(tq^2)$, Ωm
R_t = resistivity of sample, $(mL^3)/(tq^2)$, Ωm
R_w = resistivity of brine, $(mL^3)/(tq^2)$, Ωm
S_{CO2} = saturation of CO_2, fraction
S_H = saturation of hydrate, fraction
S_w = saturation of water, fraction
S_{wi} = initial saturation of water, fraction
T = temperature, T, °C
Z = impedance, $(mL^2)/(tq^2)$, Ω
ΔP = differential pressure, $m/(Lt^2)$, bar
Θ = phase angle, °
φ = porosity, fraction
φ_{eff} = effective porosity, fraction
μ = viscosity, cP

References

1. International Energy Agency (IEA/OECD), "20 years of Carbon Capture and Storage - Accelerating future deployment." Review report (2016)
2. O. Eiken, P. Ringrose, C. Hermanrud, B. Nazarian, T. A. Torp and L. Høier, "Lessons learned from 14 years of CCS operations: Sleipner, In Salah and Snøhvit." Energy Procedia **4**, 5541-5548 (2011)
3. S. Benson and D. R. Cole, "CO2 Sequestration in Deep Sedimentary Formations." *Elements* **4**, 325-331 (2008)
4. H. Koide, M. Takahashi, H. Tsukamoto and Y. Shindo, "Self-trapping mechanisms of carbon dioxide in the aquifer disposal." *Energy Conversion and Management* **36**, 505-508 (1995)
5. B. Tohidi, R. Anderson, B. Clennell, R. W. Burgass and A. Biderkab, "Visual observation of gas-hydrate formation and dissociation in synthetic porous media by means of glass micromodels." *Geology* **29**, 867-870 (2001)
6. M. Massah, D. Sun, H. Sharifi and P. Englezos, "Demonstration of gas-hydrate assisted carbon dioxide storage through horizontal injection in lab-scale reservoir." *Journal of Chemical Thermodynamics* **117**, 106-112 (2018)
7. J. Gauteplass, S. Almenningen, G. Ersland and T. Barth, "Hydrate seal formation during laboratory CO2 injection in a cold aquifer." *International Journal of Greenhouse Gas Control* **78**, 21-26 (2018)
8. S. Almenningen, J. Gauteplass, P. Fotland, G. L. Aastveit, T. Barth and G. Ersland, "Visualization of hydrate formation during CO2 storage in water-saturated sandstone." *International Journal of Greenhouse Gas Control* **79**, 272-278 (2018)
9. C. A. Rochelle, A. P. Camps, D. Long, A. Milodowski, K. Bateman, D. Gunn, P. Jackson, M. A. Lovell and J. Rees, "Can CO2 hydrate assist in the underground storage of carbon dioxide?" *Geological Society* **319**, 171-183 (2009)
10. G. E. Archie, "The Electrical Resistivity Log as an Aid in Determining Some Reservoir Characteristics." *AIME* **146**, 54-62 (1942)
11. Baker-Hughes. *Introduction to Wireline Log Analysis* (1992)
12. J. J. Arps, "The Effect of Temperature on the Density and Electrical Resistivity of Sodium Chloride Solutions." *Journal of Petroleum Technology* **5**, 17-20 (1953)
13. A. E. Cook and W. F. Waite, "Archie's Saturation Exponent for Natural Gas Hydrate in Coarse-Grained Reservoirs." *Journal of Geophysical Research: Solid Earth* **123**, 2069-2089 (2018)
14. K. A. Birkedal, G. Ersland, L. P. Hauge, A. Graue, K. Hester, J. Stevens and J. Howard, "Electrical resistivity measurements of CH4 hydrate-bearing sandstone during formation." *7th International Conference on Gas Hydrates* (2011)
15. A. E. Cook, B. I. Anderson, J. Rasmus, K. Sun, Q. Li, T. S. Collett and D. S. Goldberg, "Electrical anisotropy of gas hydrate-bearing sand reservoirs in the Gulf of Mexico." *Marine and Petroleum Geology* **34** (2012)
16. Y. F. Sun, and D. Goldberg, "Dielectric method of high-resolution gas hydrate estimation." *Geophysical Research Letters* **32** (2005)
17. T. Ramstad and H. Rueslåtten, "Pore scale numerical analysis for geological sequestration of CO_2." Technical report, 1-63 (2013)
18. C. Hågenvik, "CO2 Injection in Hydrate Bearing Sandstone with Excess Water." University of Bergen, MSc thesis (2013)
19. D. Bosch, J. Ledo, P. Queralt, F. Bellmunt, L. Luquot and P. Gouze, "Core-scale electrical resistivity tomography (ERT) monitoring of CO2–brine mixture in Fontainebleau sandstone." *Journal of Applied Geophysics* **130**, 23-36 (2016)
20. M. Han, S. Youssef, E. Rosenberg, M. Fleury and P. Levitz, "Deviation from Archie's law in partially saturated porous media: Wetting film versus disconnectedness of the conducting phase." *Physical Review E* **79** (2009)
21. J. H. Börner, V. Herdegen, J.-U. Repke and K. Spitzer, "The impact of CO2 on the electrical properties of water bearing porous media – laboratory experiments with respect to carbon capture and storage." *Geophysical Prospecting* **61**, 446-460 (2013)
22. M. Fleury and H. Deschamps, "Electrical Conductivity and Viscosity of Aqueous NaCl Solutions with Dissolved CO2." *Journal of Chemical & Engineering Data* **53**, 2505-2509 (2008)
23. E. Spangenberg and J. Kulenkampff., "Influence of methane hydrate content on electrical sediment properties." *Geophysical Research Letters* **33** (2006)
24. Y. Liu, W. Zhang, Y. Liu, S. Ren, "Experimental characterization and modelling of acoustic and electrical resistance in hydrate bearing sediments." *6th International Conference on Gas Hydrates* (2008)

25. J. H. Börner, K. Spitzer, J.-U. Repke and V. Herdegen, "The electrical conductivity of CO2-bearing pore waters at elevated pressure and temperature: a laboratory study and its implications in CO2 storage monitoring and leakage detection." *Geophysical Journal International* **203**, 1072-1084 (2015)